

Focused ion beam fabrication of Janus bimetallic cylinders acting as drift tube Zernike phase plates for electron microscopy

Cite as: J. Appl. Phys. **130**, 024507 (2021); doi: [10.1063/5.0050055](https://doi.org/10.1063/5.0050055)

Submitted: 11 March 2021 · Accepted: 22 June 2021 ·

Published Online: 12 July 2021



Paolo Rosi,^{1,2,a)}  Gian Carlo Gazzadi,² Stefano Frabboni,^{1,2}  Vincenzo Grillo,² Amir H. Tavabi,³ 
Rafal E. Dunin-Borkowski,³  and Giulio Pozzi^{3,4}

AFFILIATIONS

¹Department FIM, University of Modena and Reggio Emilia, via G. Campi 213/a, Modena 41125, Italy

²CNR-Institute of Nanoscience-S3, via G. Campi 213/a, Modena 41125, Italy

³Ernst Ruska-Centre for Microscopy and Spectroscopy with Electrons and Peter Grünberg Institute, Forschungszentrum Jülich, 52425, Jülich, Germany

⁴Department of Physics and Astronomy, University of Bologna, viale B. Pichat 6/2, Bologna 40127, Italy

^{a)}Author to whom correspondence should be addressed: paolo.rosi@nano.cnr.it

ABSTRACT

Modern nanotechnology techniques offer new opportunities for fabricating structures and devices at the micrometer and sub-micrometer level. Here, we use focused ion beam techniques to realize micrometer-sized Janus bimetallic cylinders acting as drift tube devices, which are able to impart a controlled phase shift to an electron wave. The phase shift results from the presence of contact potentials in the cylinders, in a similar manner to the electrostatic Aharonov–Bohm effect in bimetallic wires. We use electron Fraunhofer interference to demonstrate that such bimetallic structures introduce phase shifts that can be tuned to desired values by varying the dimensions of the pillars, in particular their heights. Such devices are promising for electron beam shaping and for the realization of electrostatic Zernike phase plates (i.e., devices that are able to impart a constant phase shift between an unscattered and a scattered electron wave) in electron microscopy, in particular, cryo-electron microscopy.

Published under an exclusive license by AIP Publishing. <https://doi.org/10.1063/5.0050055>

I. INTRODUCTION

Developments in state-of-the-art electron microscopes (including aberration correctors, field emission guns, and single particle detectors), in the fabrication of sub-micrometer devices [using focused ion beam (FIB) instruments, electron beam and optical lithography, etc.], and in biological specimen preparation (e.g., the use of frozen-hydrated specimens in cryo-electron microscopy) have stimulated renewed interest in using phase plates as devices that can be used to apply phase shifts to scattered electrons with respect to unscattered beams, in order to improve contrast in images of weak phase objects more efficiently than using standard methods, such as defocusing the objective lens. Phase plates are of paramount importance in cryo-electron microscopy for increasing the contrast of unstained biological molecules. Beyond electron microscopy, phase control of charged particles is relevant in the

general field of structured matter waves, in particular, for protons and light ions in the sub-MeV regime.^{1,2}

A survey of the history of phase plates has been presented by Nagayama,³ while the state of the art in the field has been reported by Glaeser,⁴ who summarized the strengths of each device, highlighted remaining problems and presented future perspectives. In his analysis, he listed electrostatic drift tubes, i.e., electrically biased drift tubes surrounded by grounded guard electrodes,⁵ as a promising approach. One of the problems with fabricating such devices is the need to connect and control the electrical bias to each nanoscale electrode, with limited space available for cabling. Here, we show how similar devices can be realized by making use of contact potential differences between metals to generate potential differences. This concept loses the advantage of tuneability but is simpler in realization and offers prospects for further reductions in device dimensions.

A desired constant phase shift can be chosen by selecting the dimensions of the device, in particular its height. A similar use of contact potentials has been reported by two groups^{6,7} for a two-metal Einzel lens configuration (Boersch phase plate),⁴ which has a different configuration from the present “drift tube” concept.

II. BASIC THEORETICAL CONSIDERATIONS

The working principle of the proposed device can be understood within the framework of the Aharonov–Bohm effect^{8–10} in its electrostatic version,^{11,12} as demonstrated previously for a bimetallic wire.^{13–16} It is straightforward to demonstrate the equivalence of the electron optical phase shifts produced by magnetic and electrostatic dipoles that are rotated with respect to each other by 90°. For a toroidal instead of a linear geometry, a circular distribution of elementary magnetic dipoles, which is shown in discrete form in Fig. 1(a), is equivalent to the circular distribution of electrostatic dipoles shown in Fig. 1(b). Each arrangement produces a constant phase shift between an electron beam passing inside and outside the toroid. On a macroscopic level, this equivalence is retained between the toroidal magnet shown in Fig. 1(c) and a cylindrical charge distribution with a radial electric dipole moment, such as the drift tube shown in Fig. 1(d).

In the present case, instead of using a dipole-based model, we consider cylindrically symmetrical charges, whose simplest electrostatic field distribution is represented by a uniformly charged ring, for which the problem of finding the electrostatic field and potential in all space has been solved.^{18–20}

In cylindrical coordinates (r, θ, z) , the potential of a ring of radius R carrying total charge Q takes the form

$$V(r, z) = \frac{1}{4\pi\epsilon_0} \frac{Q}{\sqrt{(r+R)^2 + z^2}} - \frac{2}{\pi} K \left[\frac{4rR}{(r+R)^2 + z^2} \right], \quad (1)$$

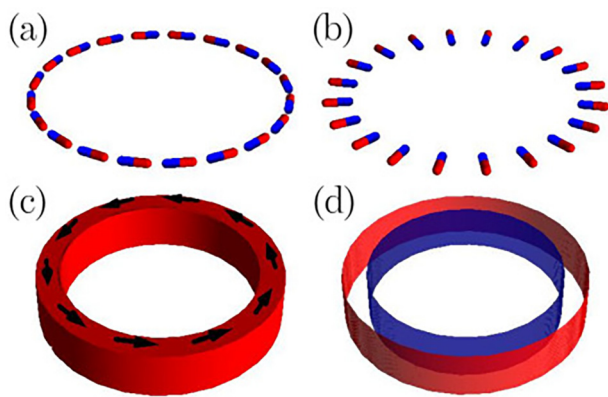


FIG. 1. Analogies between arrangements of magnetic (left) and electric (right) dipoles. (a) Toroidal magnetic flux tube and (b) toroidal ring of electrostatic dipoles, represented by discrete sets of dipoles. (c) Toroidal magnet and (d) drift tube formed from coaxial cylinders of opposite charge.

where

$$K(m) = \int_0^{\pi/2} \frac{d\theta}{\sqrt{1 - m \sin^2 \theta}} \quad (2)$$

is a complete elliptic integral of the first kind, which is defined for $0 \leq m < 1$.²¹

Just as for isolated charges,²² the electron optical phase shift of a charged ring can only be calculated if another charged ring of opposite charge is present, as convergence of the integral is then ensured by charge neutrality. In the phase object approximation, the phase shift is proportional to the projected electrostatic potential. The z coordinate is therefore not significant, but only the different radii matter. Unfortunately, the function K makes it difficult to obtain an analytical result for the phase shift by direct evaluation of the integral. Instead, numerical evaluation of the coordinate-dependent part can be carried out using Mathematica,²³ as shown in Fig. 2.

This numerical result suggests a way to find an analytical counterpart, based on the idea that the two-dimensional projected potential (and hence the electron optical phase shift) satisfies Poisson’s equation^{24–26}

$$\nabla^2 \varphi(x, y) = -C_E \frac{1}{\epsilon_0} \sigma_p(x, y), \quad (3)$$

where C_E is an interaction constant that takes a value of 7.3 rad/(V μ m) for 200 keV electrons and 10.1 rad/(V μ m) for 80 keV electrons. Furthermore, $\rho(x, y, z)$ is the charge density and $\sigma_p(x, y)$ is the projected charge density, given by the expression

$$\sigma_p(x, y) = \int_{-\infty}^{\infty} \rho(x, y, z) dz. \quad (4)$$

By applying the Gauss theorem, we can infer that the phase inside a charged ring is constant, whereas outside the ring it is equal to that obtained if the charge were concentrated at the center

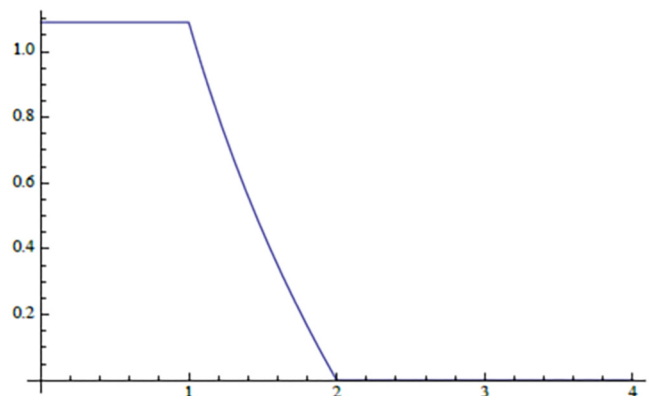


FIG. 2. Trend of the electron optical phase shift of two opposite line charges at radii 1 and 2, shown in arbitrary units.

of the ring, in the form

$$\varphi(r) = -C_E \frac{1}{4\pi\epsilon_0} Q \log\left(\frac{x^2 + y^2}{R^2}\right). \quad (5)$$

According to this equation, the phase inside the ring is constant and equal to 0.

For two oppositely charged rings with radii R_1 and $R_2 > R_1$, with the positive charge on the inner ring R_1 , the phase shift is given by the expressions

$$\varphi(r) = 0 \quad \text{for } r > R_2, \quad (6)$$

$$\varphi(r) = -C_E \frac{1}{4\pi\epsilon_0} Q \log\left(\frac{r^2}{R_2^2}\right) \quad \text{for } R_1 < r < R_2, \quad (7)$$

$$\varphi(r) = -C_E \frac{1}{4\pi\epsilon_0} Q \log\left(\frac{R_1^2}{R_2^2}\right) \quad \text{for } 0 < r < R_1. \quad (8)$$

These equations are consistent with the numerical results reported in Fig. 2. As a result of the projection of the charge described by Eq. (4), this result holds not only for a charged ring but also for the cylindrical charge distribution shown in Fig. 1(d). If the region between the charged rings is shielded by an opaque aperture, then this setup acts as a Zernike phase plate, with a phase difference that can be varied by changing the charge on the coaxial cylinders.

III. SPECIMEN PREPARATION

In order to test this proposal, we fabricated Janus bimetallic cylinders and measured their phase shifts with respect to nearby holes of nearly equal diameter. We recorded Fraunhofer images of each pair of holes, from which the phase shift of the drift tube with respect to the nearby hole could be measured in the form of a lateral displacement of the interference fringes with respect to the diffraction envelope.²⁷ This effect was enhanced by optimizing the radii of the holes and their separations.^{17,27}

An estimate of the phase difference can be obtained by assuming that the potential inside a cylinder of height h is constant and equal to the contact potential difference V_C between the two dissimilar metals, in our case Pt and Al, which is ~ 1 V.^{28,29} The corresponding phase difference is given by the expression^{17,30,31}

$$\phi = C_E V_C h. \quad (9)$$

The expected phase shift is 2π for a tube length $h \sim 0.86 \mu\text{m}$ for 200 keV electrons.

As the contact potential is affected greatly by the state of the surfaces and the purity of the materials, we chose to make a series of Janus bimetallic cylinders with nominal heights of 0, 0.5, 0.75, 2.5, and $4 \mu\text{m}$, the first of which served as a reference. We used focused ion beam (FIB) techniques in an FEI strata DB235M equipped with a Ga^+ liquid metal ion source (LMIS) operated at 30 keV to realize toroidal versions of bimetallic wires. The starting point was a commercial PELCO ultra-low-stress silicon nitride support film with nine $100 \times 100 \mu\text{m}$ windows and a membrane

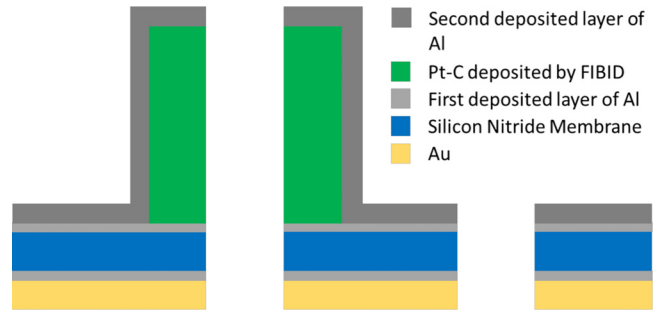


FIG. 3. Schematic diagram of the cross-sectional structures of the cylinders and adjacent holes.

thickness of 200 nm. The frame supporting the membranes was a standard 3-mm-diameter round silicon frame of thickness $200 \mu\text{m}$. We evaporated ~ 50 nm of Al onto each side of the membrane. Pairs of circular holes, with a pillar on one hole in each pair, were then fabricated in four steps to realize the cross-sectional structures shown in Fig. 3. First, Pt-C cylinders were deposited by FIBID-induced deposition (FIBID) using a Pt-organic precursor gas [trimethylmethylcyclopentadienylplatinum (IV), $(\text{CH}_3)_3\text{C}_5\text{H}_4\text{Pt}$, vaporized by heating to 44°C]. The ion beam current used during deposition was ~ 50 pA. For each cylinder, the ion beam was scanned during gas injection over a ring-shaped area with an inner radius of $1.15 \mu\text{m}$ and an outer radius of $1.5 \mu\text{m}$. Five pillars of varying height were deposited. The total scan time was ~ 1 min for the shortest pillar and ~ 9 min for the tallest pillar [Fig. 4(e)]. A distance of at

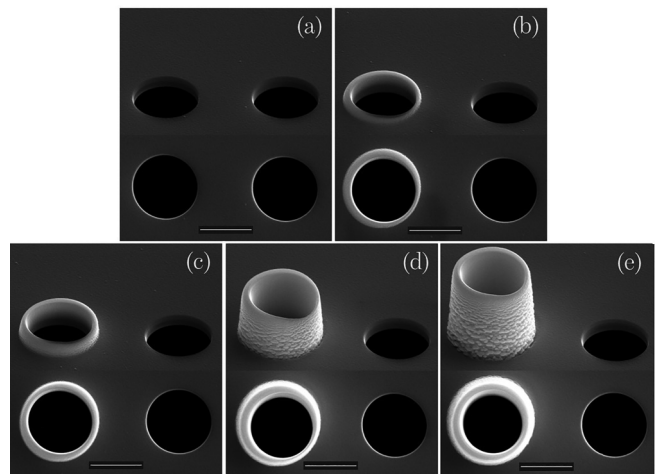


FIG. 4. SEM tilted and top views of the double circular aperture structures. One aperture in each pair takes the form of a FIBID-fabricated Al-covered Pt-C tube (beam energy 30 keV, beam current 50 pA during deposition and 100 pA during milling). Several representative values of tube height are shown. The scale bar in each image is $2 \mu\text{m}$. The measured pillar heights are (a) 0 (i.e., no pillar structure), (b) $(0.4 \pm 0.1) \mu\text{m}$, (c) $(0.7 \pm 0.1) \mu\text{m}$, (d) $(2.2 \pm 0.1) \mu\text{m}$, and (e) $(3.3 \pm 0.1) \mu\text{m}$.

least $35\ \mu\text{m}$ was maintained between pillars and no more than three pillars were deposited on each window. In the second step, a bimetallic structure was created by depositing $\sim 100\ \text{nm}$ of Al over the entire sample using thermal evaporation. In the final step, a double aperture was formed by creating pairs of holes with radii of $1.2\ \mu\text{m}$ using FIB milling, one through each tube and one adjacent to it. The distance between the centers of the adjacent holes was approximately twice the diameter of each hole. Here, the ion beam current was increased to $\sim 100\ \text{pA}$. It was found to be necessary to deposit a further $\sim 150\ \text{nm}$ of Au onto the “lower” side of the membrane using sputter coating, in order to make the support completely opaque to electrons at $200\ \text{keV}$.

Figure 4 shows scanning electron microscopy (SEM) images recorded in tilted and top view configurations. A reference structure of two holes without a fabricated pillar structure is shown in Fig. 4(a). The tilted views shown in Figs. 4(b)–4(e) allow the pillar heights to be measured. The nominal values of the heights of the pillars shown are 0.5 , 0.75 , 2.5 , and $4\ \mu\text{m}$, while the measured heights from the SEM tilted views are $(0.4 \pm 0.1)\ \mu\text{m}$, $(0.7 \pm 0.1)\ \mu\text{m}$, $(2.2 \pm 0.1)\ \mu\text{m}$, and $3.3 \pm 0.1\ \mu\text{m}$, respectively.

IV. EXPERIMENTAL RESULTS

Experiments were carried out at 80 and $200\ \text{keV}$ on a Talos F200S G2 TEM in low magnification, low angle diffraction mode

(camera length $1.4\ \text{km}$). Results obtained from the structures shown in Fig. 4 are reported in Fig. 5. Values of the phase difference were measured by performing fits to the data based on the formula

$$I(x) = b \frac{J_1^2(xD)}{(xD)^2} [1 + \mu \cos(xd + \Delta\varphi)], \quad (10)$$

which was derived by considering Fraunhofer images of two circular apertures.²⁷ The multiplicative factor is the Fourier transform of a circular aperture (i.e., an Airy disk), while the interference term in square brackets includes a damping factor μ , which accounts for partial coherence effects resulting from the finite dimensions of the electron source (i.e., spatial coherence).²⁷ J_1 is a Bessel function of the first kind, b is a fitting parameter that allows a non-normalized intensity profile to be fitted, $\Delta\varphi$ is the phase difference between the apertures, and D and d are coefficients that are proportional to the aperture diameter and separation, respectively. As a result of the high coherence of the Schottky field emission gun, the influence of spatial coherence was found to be less than 10% of the overall intensity. The values of phase difference between the two apertures, which were obtained modulo 2π from the fitting procedure, are reported in Fig. 5 on the right of each line scan plot. The Fraunhofer images and the corresponding line scans show that the

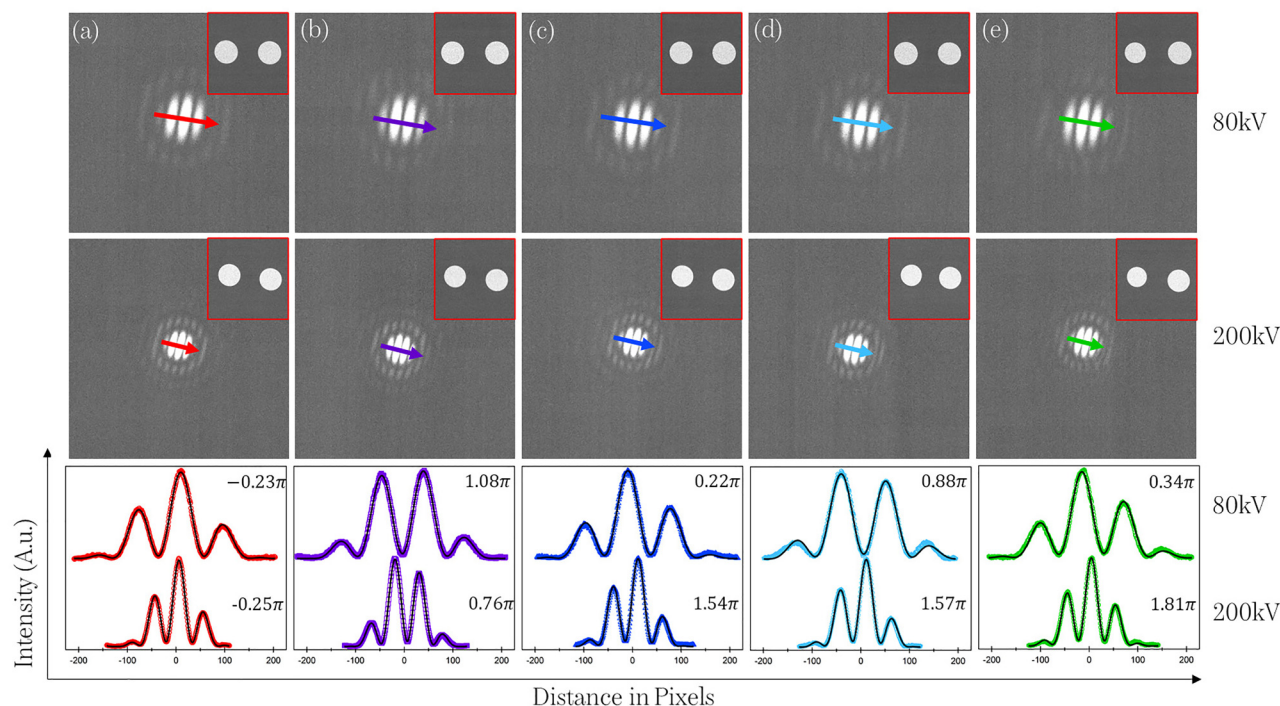


FIG. 5. TEM images and diffraction patterns of the double apertures shown in Fig. 4: (a) Reference, (b) 0.4 , (c) 0.7 , (d) 2.2 , (e) $3.3\ \mu\text{m}$. The first row shows data collected at $80\ \text{keV}$, while the second row shows data collected at $200\ \text{keV}$. Line scans of the diffraction patterns are shown in the lower two rows, with markers representing experimental data points and solid black lines fits. The direction of the line scan is marked by an arrow in each diffraction pattern. The phase differences (modulo 2π) obtained from fits to Eq. (10) are indicated in the upper right corner of each line scan.

pattern changes with pillar height due to changes in the phase difference between the holes. For the double aperture with the smallest cylinder [Fig. 5(b)], the phase difference is almost π at both accelerating voltages. A similar structure in the intensity profile can be observed for the double aperture with a pillar height of $\sim 2.2\ \mu\text{m}$ [Fig. 5(d)] at 80 keV, but not at 200 keV, which instead shows marked asymmetry, suggesting that the phase difference between the two holes is neither 0 nor 2π .

The shape of each line scan plot shows that at both accelerating voltages the reference (with no pillar on either of the holes) is slightly asymmetrical. Fits of the data to Eq. (10) indicate that at both accelerating voltages the phase difference is almost $-\frac{\pi}{4}$. This unexpected effect, in the absence of a pillar, probably results from the metal-insulating structure of the holes, as well as some asymmetry between them resulting from the fabrication process. Similar behavior was recently observed in another paper with circularly symmetrical structures built on a silicon nitride supporting layer.³² Metal deposition reduced charging effects but did not completely remove them.

We plotted the total phase difference as a function of cylinder height. The total phase difference was calculated by adding an integer multiple of 2π to each phase difference value obtained from the fitting procedure so that $\Delta\varphi_{\text{tot}} = \Delta\varphi_{\text{fit}} + n2\pi$. The value of n for each pillar height was chosen to be the rounded-off integer result of the division $h_{\text{pillar}}/h_{2\pi}$. We estimated an initial plausible value of $h_{2\pi}$ for each accelerating voltage from the trend of the fitted phase difference reported in Fig. 5. In Fig. 5(c), the phase difference at 80 keV should have already surpassed 2π since that calculated from the fit is 0.22π , while it is close to being reached at 200 keV. The two first guesses were therefore $h_{2\pi-80\text{ keV}} \approx 0.6\ \mu\text{m}$ and $h_{2\pi-200\text{ keV}} \approx 0.8\ \mu\text{m}$. We then fitted the linear function

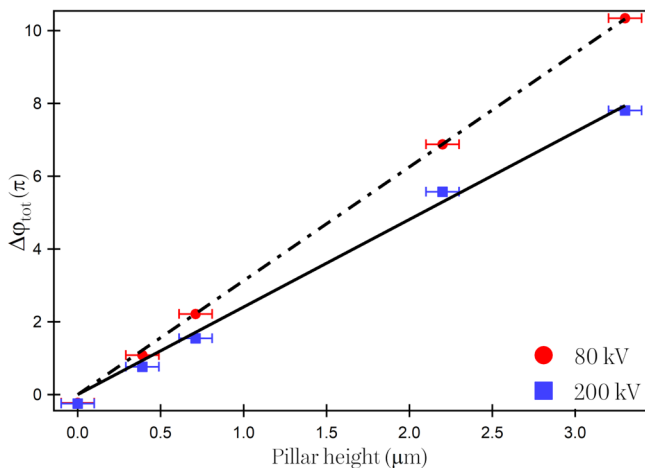


FIG. 6. Total phase difference plotted as a function of pillar height at 200 keV (blue squares) and 80 keV (red circles). We added suitable multiples of 2π to the experimental phase differences obtained from fitting the data. We fitted our data with a linear fitting function, which first allows us to estimate the height corresponding to a 2π phase shift and then provides an approximate value of the contact potential.

$\Delta\varphi_{\text{tot}} = \beta h_{\text{pillar}}$ to the data and tried other values of $h_{2\pi}$ to minimize χ^2 (evaluated using Pearson's χ^2 test³³). The physical meaning of β can be understood when we compare the linear fitting function to Eq. (9) so that $\beta = C_E V_{C\text{exp}}$. The results are shown in Fig. 6. However, it is important to note that the result is not unequivocal, since we have a small number of data points.

The angular coefficient for the linear fit with the smallest value of χ^2 is $\beta_{200\text{ keV}} = (2.40 \pm 0.06) \frac{\pi}{\mu\text{m}}$ for the 200 keV series, while $\beta_{80\text{ keV}} = (3.13 \pm 0.03) \frac{\pi}{\mu\text{m}}$ at 80 keV. The ratio between the two angular coefficients is $r_\beta = \frac{\beta_{80\text{ keV}}}{\beta_{200\text{ keV}}} \approx 1.3$, which is consistent with the ratio between the interaction constants $r_{C_E} = \frac{C_E-80\text{ keV}}{C_E-200\text{ keV}} = 1.3836$. From the two angular coefficients, it is also possible to estimate the pillar height corresponding to a full 2π phase shift, where $h_{2\pi\text{fit}} = \frac{2\pi}{\beta}$ so that for 200 keV electrons the resulting pillar height is $\sim 0.83\ \mu\text{m}$, while for 80 keV electrons the pillar height is $\sim 0.64\ \mu\text{m}$. By comparing $h_{2\pi}$ resulting from fitting the 200 keV data to the expected value [$\sim 0.86\ \mu\text{m}$, as estimated from Eq. (9)], it can be seen that the two values are in agreement within a small margin of error. We can then determine an approximate value for the potential difference experienced by the electrons when they travel through the pillar to be $V_{C\text{exp}} \approx 1.04\ \text{V}$.

V. CONCLUSIONS

The fitted values of the phase difference shown in Fig. 5 are consistent with the generation of constant phase shifts by Janus bimetallic cylindrical structures that behave as drift tubes. More systematic experiments are required in the future to assess the influence on the phase shift of experimental parameters associated with the fabrication process, as well as possible effects of electron beam induced charging of both the structures and their supports. When improved control of the phase shift is achieved, it may be possible to use structures such as Zernike phase plates in transmission electron microscopy, as they are more compact than tunable drift tube devices and therefore promise to allow a greater number of spatial frequencies to contribute to phase contrast images.

Beyond their use as Zernike phase plates, we foresee the application of such bimetallic devices for different forms of electron beam shaping. For example, they could be used to replace electrostatic elements in applications such as spiral phase plates,^{34–38} Hilbert phase plates, and electrostatic orbital angular momentum sorters.^{39,40} They could also be used to replace electrostatic phase plates for conformal mapping operations.⁴¹ A two-dimensional array of such cylinders could be used to produce an arbitrary phase landscape without the problems that come with using material-based holograms. A similar concept was recently proposed for pixelated programmable phase plates.^{32,42} When using bimetallic cylinders, the loss of *in situ* programmability would be compensated by the ability to fabricate a greater number of pixels per unit area. It is possible to reduce by a factor of 2 the radial dimension of the bimetallic hollow cylinder. When coupled with the lack of necessity of bringing contact lines to each pixel, this results in a greater pixel density with respect to the corresponding tunable device. A clear advantage should be the possibility to better reproduce a desired phase profile. Apart from a loss of intensity from the increase in pixel density, the main limiting factors would be the width of the cylinder walls, which cannot be reduced using the present

technique, as well as the decoherence effect (now at 10%), which would affect the beam more strongly when using a smaller hole.

Whereas the former applications belong to the emerging and promising field of structured electron beams, phase plates also play an outstanding role in the field of electron microscopy, as pointed out in a recent review paper by Malac *et al.*⁴³ As pointed out in Sec. I, phase plates substantially improve the experimental observation of biological samples, which are radiation sensitive and/or provide very weak contrast, thereby allowing for the elimination of staining by heavy metals. In addition to huge potential in life science applications, materials science and applied physics future applications include the investigation of long-range magnetic and electric fields and semiconductor devices. In the case of magnetic materials, the in focus observation of both the magnetic field and the sample microstructure allows improved correlation between them, as well as the potential to image dynamic phenomena.

ACKNOWLEDGMENTS

P.R. and S.F. acknowledge the staff at the CIGS facility in Modena for helping in setting up the TEM experiments. The research leading to these results has received funding from the European Union's Horizon 2020 Research and Innovation Programme under Grant Agreement Nos. 766970 Q-SORT (H2020-FETOPEN-1-2016-2017) and 823717 (project ESTEEM3).

DATA AVAILABILITY

The data that support the findings of this study are available from the corresponding author upon reasonable request.

REFERENCES

- ¹C. Shukla and A. Das, "Ion vortex beam," [arXiv:1711.02896](https://arxiv.org/abs/1711.02896) (2017).
- ²G. M. Vanacore, G. Berruto, I. Madan, E. Pomarico, P. Biagioni, R. J. Lamb, D. McGrouther, O. Reinhardt, I. Kammer, B. Barwick, H. Larocque, V. Grillo, E. Karimi, F. J. García de Abajo, and F. Carbone, "Ultrafast generation and control of an electron vortex beam via chiral plasmonic near fields," *Nat. Mater.* **18**, 573–579 (2019).
- ³K. Nagayama, "Another 60 years in electron microscopy: Development of phase-plate electron microscopy and biological applications," *J. Electron Microsc. (Tokyo)* **60**, S43–S62 (2011).
- ⁴R. M. Glaeser, "Invited review article: Methods for imaging weak-phase objects in electron microscopy," *Rev. Sci. Instrum.* **84**, eid111101 (2013).
- ⁵R. Cambie, K. H. Downing, D. Typke, R. M. Glaeser, and J. Jin, "Design of a microfabricated, two-electrode phase-contrast element suitable for electron microscopy," *Ultramicroscopy* **107**, 329–339 (2007).
- ⁶J. Perry-Houts, B. Barton, A. Schmid, N. Andresen, and C. Kisielowski, "Novel long-lived electrostatic work function phase plates for TEM," *Microsc. Microanal.* **18**, 476–477 (2012).
- ⁷H. Tamaki, H. Kasai, K. Harada, Y. Takahashi, and R. Nishi, "Development of a contact-potential-type phase plate," *Microsc. Microanal.* **19**, 1148–1149 (2013).
- ⁸Y. Aharonov and D. Bohm, "Significance of electromagnetic potentials in the quantum theory," *Phys. Rev.* **115**, 485–491 (1959).
- ⁹Y. Aharonov, "Non-local phenomena and the Aharonov-Bohm effect," in *Proceedings of the International Symposium on Foundations of Quantum Mechanics (ISQM'83)*, edited by S. Kamefuchi, H. Ezawa, Y. Murayama, M. Namiki, S. Nomura, Y. Ohnuki, and T. Yajima (Physical Society of Japan, Tokyo, 1984), pp. 10–19.
- ¹⁰S. Olariu and I. I. Popescu, "The quantum effects of electromagnetic fluxes," *Rev. Mod. Phys.* **57**, 339–436 (1985).
- ¹¹T. H. Boyer, "Classical electromagnetic deflections and lag effects associated with quantum interference pattern shifts: Considerations related to the Aharonov-Bohm effect," *Phys. Rev. D* **8**, 1679–1693 (1973).
- ¹²T. H. Boyer, "Semiclassical explanation of the Matteucci-Pozzi and Aharonov-Bohm phase shifts," *Found. Phys.* **32**, 41–49 (2002).
- ¹³G. Matteucci, G. F. Missiroli, and G. Pozzi, "A new electrostatic phase-shifting effect," *Ultramicroscopy* **10**, 247–251 (1982).
- ¹⁴G. Matteucci and G. Pozzi, "New diffraction experiment on the electrostatic Aharonov-Bohm effect," *Phys. Rev. Lett.* **54**, 2469–2472 (1985).
- ¹⁵G. Matteucci, F. F. Medina, and G. Pozzi, "Electron-optical analysis of the electrostatic Aharonov-Bohm effect," *Ultramicroscopy* **41**, 255–268 (1992).
- ¹⁶G. Matteucci, G. F. Missiroli, and G. Pozzi, "Electron holography of long-range electrostatic fields," in *Advances in Imaging and Electron Physics*, edited by P. W. Hawkes (Elsevier, 2002), Vol. 122, pp. 173–249.
- ¹⁷G. Pozzi, "Particles and waves in electron optics and microscopy," in *Advances in Imaging and Electron Physics*, edited by P. W. Hawkes (Academic Press, New York, 2016), Vol. 194.
- ¹⁸E. Ball, "Potential from a ring of charge," *Proc. Inst. Electrical Eng.* **124**, 664 (1977).
- ¹⁹F. R. Zypman, "Off-axis electric field of a ring of charge," *Am. J. Phys.* **74**, 295–300 (2006).
- ²⁰O. Ciftja, A. Babineaux, and N. Hafeez, "The electrostatic potential of a uniformly charged ring," *Eur. J. Phys.* **30**, 623–627 (2009).
- ²¹G. B. Arfken and H.-J. Weber, *Mathematical Methods for Physicists*, 6th ed. (Elsevier, Boston, 2005).
- ²²A. H. Tavabi, V. Migunov, C. Dwyer, R. E. Dunin-Borkowski, and G. Pozzi, "Tunable caustic phenomena in electron wavefields," *Ultramicroscopy* **157**, 57–64 (2015).
- ²³S. Wolfram, *The Mathematica Book*, 4th ed. (Wolfram Media, Champaign, IL, 1999).
- ²⁴M. Beleggia, T. Kasama, R. E. Dunin-Borkowski, S. Hofmann, and G. Pozzi, "Direct measurement of the charge distribution along a biased carbon nanotube bundle using electron holography," *Appl. Phys. Lett.* **98**, 243101 (2011).
- ²⁵C. Gatel, A. Lubk, G. Pozzi, E. Snoeck, and M. Hÿtch, "Counting elementary charges on nanoparticles by electron holography," *Phys. Rev. Lett.* **111**, 025501 (2013).
- ²⁶M. Beleggia, L. Gontard, and R. Dunin-Borkowski, "Local charge measurement using off-axis electron holography," *J. Phys. D: Appl. Phys.* **49**, 294003 (2016).
- ²⁷M. Born and E. Wolf, *Principles of Optics: Electromagnetic Theory of Propagation, Interference and Diffraction of Light*, 4th ed. (Pergamon Press, Oxford, 1969).
- ²⁸H. B. Michaelson, "The work function of the elements and its periodicity," *J. Appl. Phys.* **48**, 4729–4733 (1977).
- ²⁹J. R. Rumble, D. R. Lide, and T. J. Bruno, *CRC Handbook of Chemistry and Physics: A Ready-reference Book of Chemical and Physical Data* (CRC Press, 2020).
- ³⁰H. Kohl and L. Reimer, *Transmission Electron Microscopy: Physics of Image Formation* (Springer, 2008).
- ³¹G. Pozzi, M. Beleggia, T. Kasama, and R. E. Dunin-Borkowski, "Interferometric methods for mapping static electric and magnetic fields," *C. R. Phys.* **15**, 126–139 (2014).
- ³²P. Thakkar, V. A. Guzenko, P.-H. Lu, R. E. Dunin-Borkowski, J. P. Abrahams, and S. Tsujino, "Fabrication of low aspect ratio three-element Boersch phase shifters for voltage-controlled three electron beam interference," *J. Appl. Phys.* **128**, 134502 (2020).
- ³³P. Bevington and D. Robinson, *Data Reduction and Error Analysis for the Physical Sciences* (McGraw-Hill Education, 2003).
- ³⁴S. Fürhapter, A. Jesacher, C. Maurer, S. Bernet, and M. Ritsch-Marte, "Spiral phase microscopy," in *Advances in Imaging and Electron Physics*, edited by P. W. Hawkes (Elsevier, 2007), Vol. 146, pp. 1–56.
- ³⁵R. Juchtmans, L. Clark, A. Lubk, and J. Verbeeck, "Spiral phase plate contrast in optical and electron microscopy," *Phys. Rev. A* **94**, 023838 (2016).

- ³⁶R. Juchtmans and J. Verbeeck, “Local orbital angular momentum revealed by spiral-phase-plate imaging in transmission-electron microscopy,” *Phys. Rev. A* **93**, 023811 (2016).
- ³⁷G. Pozzi, P.-H. Lu, A. H. Tavabi, M. Duchamp, and R. E. Dunin-Borkowski, “Generation of electron vortex beams using line charges via the electrostatic Aharonov-Bohm effect,” *Ultramicroscopy* **181**, 191–196 (2017).
- ³⁸A. H. Tavabi, H. Larocque, P.-H. Lu, M. Duchamp, V. Grillo, E. Karimi, R. E. Dunin-Borkowski, and G. Pozzi, “Generation of electron vortices using nonexact electric fields,” *Phys. Rev. Res.* **2**, 013185 (2020).
- ³⁹G. Pozzi, V. Grillo, P.-H. Lu, A. H. Tavabi, E. Karimi, and R. E. Dunin-Borkowski, “Design of electrostatic phase elements for sorting the orbital angular momentum of electrons,” *Ultramicroscopy* **208**, 112861 (2020).
- ⁴⁰A. H. Tavabi, P. Rosi, E. Rotunno, A. Roncaglia, L. Belsito, S. Frabboni, G. Pozzi, G. C. Gazzadi, P.-H. Lu, R. Nijland *et al.*, “Experimental demonstration of an electrostatic orbital angular momentum sorter for electron beams,” *Phys. Rev. Lett.* **126**, 094802 (2021).
- ⁴¹G. Ruffato, E. Rotunno, L. M. C. Giberti, and V. Grillo, “Arbitrary conformal transformations of wave functions,” *Phys. Rev. Appl.* **10**, 1–11 (2021).
- ⁴²J. Verbeeck, A. Béch , K. M ller-Caspary, G. Guzzinati, M. A. Luong, and M. Den Hertog, “Demonstration of a 2×2 programmable phase plate for electrons,” *Ultramicroscopy* **190**, 58–65 (2018).
- ⁴³M. Malac, S. Hettler, M. Hayashida, E. Kano, R. F. Egerton, and M. Beleggia, “Phase plates in the transmission electron microscope: Operating principles and applications,” *Microscopy* **70**, 75–115 (2021).